

Cite this: RSC Advances, 2011, 1, 1542–1553

www.rsc.org/advances

PAPER

Well-crystallized square-like 2D BiOCl nanoplates: mannitol-assisted hydrothermal synthesis and improved visible-light-driven photocatalytic performance†

Jinyan Xiong,‡ Gang Cheng,‡ Guangfang Li, Fan Qin and Rong Chen*

Received 22nd June 2011, Accepted 18th August 2011

DOI: 10.1039/c1ra00335f

Well-crystallized square-like bismuth oxychloride (BiOCl) nanoplates were successfully synthesized by a facile and environmentally friendly hydrothermal process in mannitol solution. The product was characterized by X-ray powder diffraction (XRD), scanning electron microscopy (SEM), transmission electron microscopy (TEM), selected area electron diffraction (SAED), Raman spectroscopy, UV-vis diffuse reflection spectroscopy (DRS) and nitrogen adsorption. It was found that mannitol played a key role in the formation of square-like BiOCl nanoplates and the possible growth mechanism was also discussed. The photocatalytic activity of prepared BiOCl nanoplates was determined by the degradation of Rhodamine B (RhB) under visible light irradiation. The square-like BiOCl nanoplates exhibited excellent visible-light-driven photocatalytic efficiency, which was much higher than that of commercial BiOCl and TiO₂ (anatase). The remarkable visible-light photocatalytic activity was mainly attributed to the synergistic effect of the layered structure and the strong adsorption of RhB dye upon the BiOCl nanoplates, which might allow more efficient transport of the injected electrons. A possible dye-sensitized photocatalytic degradation process (photosensitization pathway) was proposed.

1. Introduction

Photocatalysis was considered a “green” technology for the treatment of organic contaminates and waste water.^{1,2} TiO₂ was undoubtedly the most excellent photocatalyst for the degradation of organic pollutants under UV irradiation.^{3,4} Unfortunately, UV light accounts for less than 5% of the solar energy that reaches the earth surface, which limited the effective use of sunlight for the photocatalytic degradation of organic pollutants. Over the past few years, tremendous efforts have been made to develop visible-light-driven photocatalysts, which could maximally utilize the clean, safe and abundant solar energy.^{5,6} However, there are few successful examples which are visible-light active in the photocatalytic oxidative decomposition of organic contaminants.

Bismuth oxychloride (BiOCl), as one of the important main group multicomponent V-VI-VII semiconductors, has drawn considerable attention for its potential applications as a novel photocatalyst due to its unique layered structures and high chemical stability.⁷ BiOCl is known to be a tetragonal layered

structure consisting of [Cl–Bi–O–Bi–Cl] sheets stacked together by the nonbonding interaction through the Cl atoms along the *c*-axis. It is also the simplest member of Sillén family expressed by [M₂O₂][Cl_{*m*}] or [M₃O_{4+n}][Cl_{*m*}] (*m* = 1–3).⁸ The strong internal static electric fields perpendicular to the Cl layer and the bismuth oxide-based fluorite-like layer enable the effective separation of the photoinduced electron-hole pairs, and result in a high photocatalytic performance.^{7,9–11} Owing to its unique properties and promising applications, there is considerable interest in the synthesis and investigation of photocatalytic performances of BiOCl nanostructures. Various BiOCl nanostructures including nanobelts,¹² nanowires,¹³ nanofibers,¹⁴ nanoplates,^{15–17} nanosheets,^{17–19} nanoflakes^{16,20} and 3D hierarchical nanostructures^{8,15,21–23} have been fabricated *via* different synthetic routes, such as template-assisted synthesis, hydro-/solvothermal routes, sonochemistry, ionothermal synthesis and so on. Among them, two-dimensional (2D) BiOCl nanostructures such as nanoplates and nanosheets are of great importance because of their excellent optical and catalytic properties, and potential uses for building blocks for advanced materials and devices, which mainly arise from their large surface areas, perfect crystallinity and structured anisotropy. However, BiOCl products with well-defined 2D morphologies and well-crystallized nanostructures are still hard to obtain and highly desired. Up to now, although several synthetic methods for 2D BiOCl nanosheets and nanoplates were reported in the literature, it is still a big challenge to develop a new environmentally friendly route to prepare 2D BiOCl

Key Laboratory for Green Chemical Process of Ministry of Education and School of Chemical Engineering and Pharmacy, Wuhan Institute of Technology, Xiongchu Avenue, Wuhan, 430073, PR China.

E-mail: rchenhku@hotmail.com; Fax: (+86)2787194465;

Tel: (+86)13659815698

† Electronic supplementary information (ESI) available. See DOI: 10.1039/c1ra00335f

‡ These authors made equal contributions to this work.

nanostructures with well defined shapes and good crystallinity and investigate their photocatalytic properties. On the other hand, most of the photocatalytic investigations of the BiOCl nanostructures focused on their photocatalytic performance under UV light irradiation, which severely hindered BiOCl to be effectively used in a practical way. Inspired by the big challenge and previous work, we reported the mannitol-assisted hydrothermal synthesis of well-crystallized BiOCl nanoplates with square-like morphology, as well as their improved visible-light-driven photocatalytic ability for the degradation of Rhodamine B (RhB) compared with that of commercial BiOCl and TiO₂. Based on the time and solvent-dependent experiments results, a possible formation mechanism was proposed. The photodegradation mechanism of BiOCl under visible light irradiation was also discussed. To the best of our knowledge, the use of mannitol, an environment-friendly and economical biopolyol, in the controlled synthesis of 2D BiOCl nanoplates has never been reported. Moreover, there are few investigations of visible-light-driven photocatalytic activities as well as the photodegradation mechanism of BiOCl nanostructures.

2. Experimental

2.1 Chemicals

Bismuth nitrate pentahydrate ($\text{Bi}(\text{NO}_3)_3 \cdot 5\text{H}_2\text{O}$), sodium chloride (NaCl), mannitol, ethylene glycol (EG), diethylene glycol (DEG) were purchased from Sinopharm Chemical Reagent Co., Ltd. (Shanghai, China). Commercial BiOCl powders were purchased from Sigma-Aldrich. TiO₂ (anatase) was purchased from Wan Jing New Material Co., Ltd. (Hangzhou, China). Rhodamine B (RhB) was purchased from Aladdin. All the reagents were analytical grade and used directly without further purification.

2.2 Synthesis

In a typical experiment, 0.486 g $\text{Bi}(\text{NO}_3)_3 \cdot 5\text{H}_2\text{O}$ (1 mmol) was put into 50 mL round-bottom flask which contained 25 mL 0.1 M mannitol solution (0.455 g mannitol in 25 mL H₂O). The mixture was stirred and sonicated until the $\text{Bi}(\text{NO}_3)_3 \cdot 5\text{H}_2\text{O}$ was dissolved, followed by the addition of 5 mL saturated sodium chloride solution, resulting in the formation of a uniform white suspension. Then the mixture was transferred to a Teflon-lined stainless steel autoclave to perform hydrothermal process at 150 °C for 3 h. After cooling down to room temperature, the solid product was collected by centrifugation and washed with deionized water five times to remove any possible remaining impurity. The samples were finally dried in a desiccator for few days at room temperature for further characterization. In order to investigate the role of mannitol molecules in the synthesis, other BiOCl samples were also prepared under identical conditions by using EG, DEG and H₂O as the solvent, respectively, instead of mannitol solution.

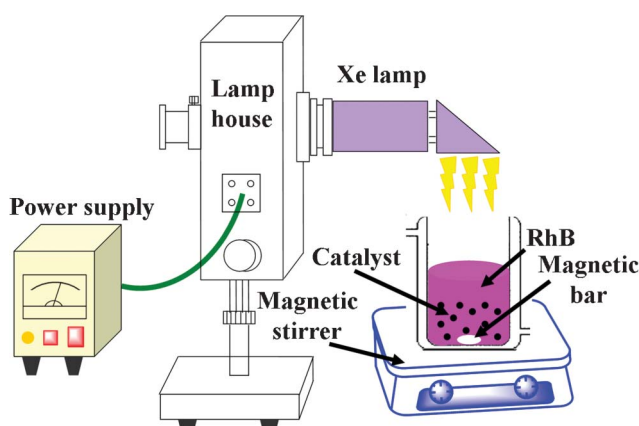
2.3 Characterization

Powder X-ray diffraction (XRD) was carried on Bruker axs D8 Discover ($\text{Cu}-\text{K}\alpha = 1.5406 \text{ \AA}$). The scanning rate is 1° min^{-1} in the 2θ range from 10 to 80 degree. SEM images were taken on a Hitachi S-4800 FEG scanning electron microscope operating at 5 eV. TEM, HRTEM images and SAED pattern were recorded

on a Philips Tecnai G2 20 transmission electron microscope, using an accelerating voltage of 200 kV. The samples for TEM observations were prepared by dispersing some of the solid products into ethanol and then sonicated for about 30 s. A few drops of the suspension were deposited on the copper grid, which was then put into a desiccator. The energy-dispersive X-ray spectrum (EDX) analysis was performed on an Oxford Instruments INCA with a scanning range from 0 to 20 keV. UV-vis diffuse reflectance spectra (DRS) were recorded on a UV-vis spectrometer (Shimadzu UV-2550) using BaSO₄ as a reference and were converted from reflection to absorbance by the Kubelka–Munk method. Raman spectra were measured using a WITec-Alpha confocal micro-Raman system under the back-scattering geometric configuration at room temperature. The excitation light was the 514.5 nm line of an Ar⁺ laser with 30 mW output power. The Brunauer–Emmett–Teller (BET) specific surface area of the powders was analyzed by nitrogen adsorption in a Micromeritics ASAP 2020 nitrogen adsorption apparatus (USA). All the as-prepared samples were degassed at 150 °C for 4 h prior to nitrogen adsorption measurements.

2.4 Photocatalytic activity test

The photocatalytic activities of the square-like BiOCl nanoplates were evaluated by the degradation of RhB under visible light irradiation of a 500 W Xe lamp with a 400 nm cutoff filter. The reaction cell was placed in a sealed black box of which the top was opened and the cutoff filter was placed to provide visible light irradiation (Scheme 1). In each experiment, different amounts of photocatalysts (0.01, 0.03, 0.05 and 0.1 g) were added into 100 mL RhB solution with a concentration of $10^{-5} \text{ mol L}^{-1}$. Prior to irradiation, the suspensions were stirred in the dark for 30 min to reach adsorption-desorption equilibrium. After that, the solution was exposed to visible light irradiation with magnetic stirring. At each irradiation time interval, 3 mL of the suspensions were collected and the slurry samples, including the photocatalyst and RhB solution were centrifuged (10 000 rpm, 10 min) to remove the photocatalyst particles. The solutions were analyzed by a Shimadzu UV2800 spectrophotometer, and the characteristic absorption of RhB at 554 nm was used to monitor the photocatalytic degradation. All of the measurements were carried out at room temperature. To



Scheme 1 Schematic illustration of the photocatalytic testing setup.

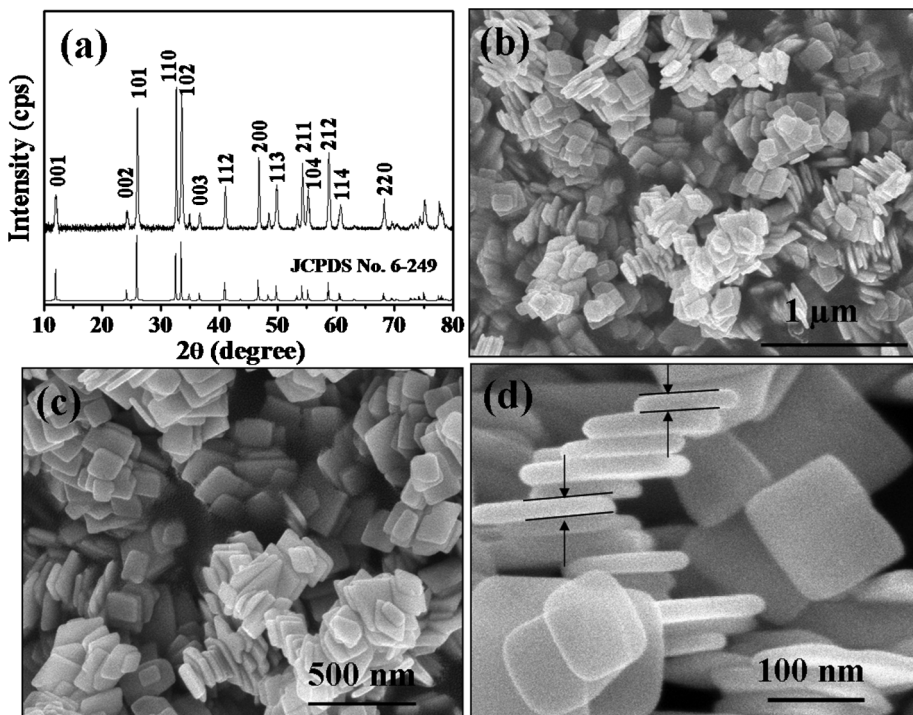


Fig. 1 XRD pattern (a) and SEM images (b–d) of the as-synthesized square-like BiOCl nanoplates prepared in mannitol solution.

compare with the photocatalytic activities of the square-like BiOCl nanoplates, the photocatalytic degradation over different photocatalysts (commercial BiOCl and TiO₂) were also performed under identical conditions.

3. Result and discussion

3.1 Structure and morphology

The purity and crystallinity of the as-synthesized product was examined by powder XRD analysis. Fig. 1a showed the typical XRD pattern of the as-synthesized product prepared in 0.1 M mannitol solution. As shown in Fig. 1a, all the diffraction peaks could be perfectly indexed to the tetragonal phase of BiOCl (cell constants $a = 3.891 \text{ \AA}$, $c = 7.369 \text{ \AA}$, JCPDS No. 6-249). No other diffraction peaks were detected, indicating of the high purity of BiOCl. The intense and sharp diffraction peaks suggested that the as-synthesized product was well-crystallized. The strongest diffraction peak at around 32.5° corresponded to the (110) plane. Fig. 1b–d showed SEM images of the BiOCl product prepared in 0.1 M mannitol solution. The low-magnification SEM image of Fig. 1b revealed that the product was composed of a large amount of well-defined square-like nanoplates. The magnified images of Fig. 1c and 1d showed that all the nanoplates had a square-like morphology, which were 100–200 nm in width and 20–30 nm in thickness.

The morphology and structure of the square-like BiOCl nanoplates were further characterized by TEM, HRTEM images and SAED patterns. As shown in Fig. 2, square-like nanoplates were found in the whole sample. It was also clearly observed that the well-defined square-like BiOCl nanoplates were 100–200 nm in width and 20–30 nm in thickness, which was in good agreement with the SEM observation. The SAED pattern (insert

of Fig. 2a) of BiOCl nanoplates revealed several diffraction rings, which were the sum of the diffraction patterns of different individual BiOCl nanoplates, indicating of good crystallinity. Fig. 2d showed clear lattice fringes of the side face of a single BiOCl nanoplate with d -spacing of 0.734 nm corresponding to the (001) lattice plane, which also suggested that the BiOCl nanoplates were well-crystallized and had a high order of crystallinity. A corresponding SAED pattern (Fig. 2e) of a single BiOCl nanoplate was further examined and its unique pattern of diffraction spots could readily be indexed to the (110) and (200) plane, which confirmed its single crystal structure. A typical HRTEM image of Fig. 2f revealed that the well-resolved interplanar d -spacing of 0.276 nm corresponded to the (110) lattice plane. The HRTEM and SAED analysis indicated that the preponderant growth direction of square-like BiOCl nanoplates was the [001] orientation, which was parallel to the (110) and (200) planes. The EDX spectrum was also used to analyze the elemental compositions of the as-synthesized square-like BiOCl nanoplates. The Bi, O and Cl signals observed indicated that the samples were composed of Bi, O and Cl, which was in good agreement with the XRD result (Fig. S1, ESI†).

3.2 Formation mechanism

BiOCl has a known tetragonal structure with lattice constants of $a = 3.890 \text{ \AA}$ and $c = 7.370 \text{ \AA}$, and a tetragonal PbFCl[−]-type structure with a space group of P4/nmm.²⁴ Its layered structure was constructed by the combination of the Cl ion layer and the metal-oxygen (Bi-O) layer.^{16,25,26} Fig. 3 showed the structure model of BiOCl crystal. In the structure, the O, Bi and Cl ions stack layer upon layer in planes perpendicular to the c axis, in which the spatial location of the Bi, O and Cl atoms (Bi at 0, 0.5, 0.171; O at 0, 0, 0; Cl at 0, 0.5, 0.65) were determined by

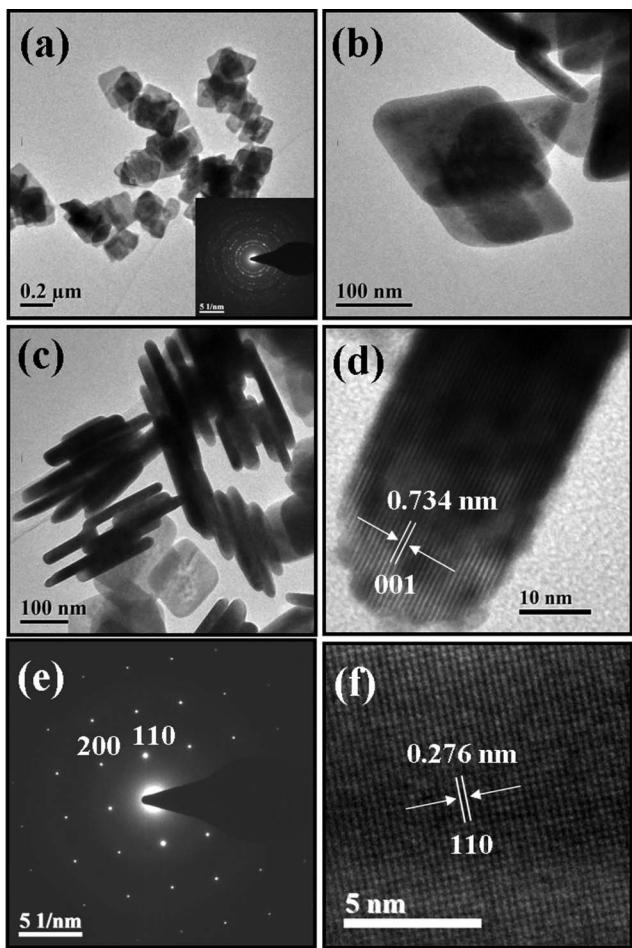


Fig. 2 TEM (a–c), HRTEM (d and f) images and SAED patterns (inset of a and e) of the as-synthesized square-like BiOCl nanoplates prepared in mannitol solution.

simulating the XRD pattern of bulk Bismocite.²⁴ It also indicated that the stacking sequence of the crystal was Cl–Bi–O–Bi–Cl Cl–Bi–O–Bi–Cl, which could be considered as [Cl–Bi–O–Bi–Cl] layers. Furthermore, the interactions within the Cl–Bi–O–Bi–Cl layers were covalent bonds, whereas the [Cl–Bi–O–Bi–Cl] layers were stacked together by the Van der Waals forces (nonbonding interaction) through the Cl atoms along the *c*-axis and strong interlayer bonding in the (001) plane.^{7,23,27} Hence, these [Cl–Bi–O–Bi–Cl] layers tended to form layered structures, such as sheets or plates with a high aspect ratio. In other words, the layered structure of bismuth oxychloride suggested that 2D laminar BiOCl nanoplates could easily be formed under appropriate conditions. It was believed that the successful synthesis of nanostructures in a solution-based system depended on the intrinsic structure of the target compounds. Meanwhile, it also required more fastidious control of the growth parameters such as the reaction time, solvent, organic additives, and so forth.^{28–33} It was favorable to understand the formation of the nanostructures by investigating the influence of experimental parameters on the morphology and structure. In order to obtain insights into the formation process of the square-like BiOCl nanoplates, control experiments were conducted by varying the reaction time and solvent. Fig. 4 showed the XRD patterns, SEM and TEM images of the BiOCl products obtained in

mannitol solution at different reaction time. As shown in Fig. 4a–d, all the observed diffraction patterns could be indexed to the tetragonal structure of BiOCl (JCPDS No. 6-249). In addition, the diffraction peak intensity of the (110) plane in the XRD patterns was relatively stronger than other planes. Before hydrothermal treatment, the diffraction peaks were relatively broader than those of the products after hydrothermal process, indicative of poor crystallinity and small particle size. With the increase of hydrothermal reaction time, the diffraction peaks became sharper and sharper, suggesting an improvement in the crystallinity.

SEM images and TEM images of BiOCl products at different reaction time demonstrated that the reaction time had a significant influence on the morphologies of the final products. As shown in Fig. 4e and 4i, irregular tiny crystals of about 20 nm were formed at the initial stage of the hydrothermal reaction, which was in good agreement with the XRD result (Fig. 4a). After 0.5 h hydrothermal treatment, the tiny BiOCl nanocrystals evolved into laminar nanostructures of irregular circular-like nanoplates, as depicted in Fig. 4f and 4j. It revealed that the larger irregular nanoplates grew at the cost of the smaller particles. When the reaction time was extended to 1.5 h, the samples were mainly composed of regular square-like nanoplates with explicit edges and a small amount of irregular nanoplates were also found (Fig. 4g and 4k). However, there was no obvious difference in morphology when the reaction time was prolonged to 6 h, compared with the product obtained by 3 h hydrothermal process (Fig. 4h and 4l). The results indicated that square-like nanoplates were fabricated through the slowly layered growth of tiny crystalline nuclei under hydrothermal conditions and a 3 h reaction time was enough for the formation of square-like nanoplates.

In the literature, EG or DEG was usually used as a solvent for the synthesis of different bismuth-containing nanostructures such as Bi₂WO₆,³⁴ (BiO)₂CO₃,³⁵ BiOCOOH,³⁶ Bi₂S₃,³⁷ and so forth. To investigate the function of mannitol in the formation of the square-like BiOCl nanoplates, EG, DEG and deionized water were also used as the solvent, instead of 0.1 M mannitol, to synthesize the BiOCl product under identical experimental conditions. As shown in the XRD spectra (Fig. 5a, 5c and 5e), the pure BiOCl product was also obtained in EG, DEG and deionized water after 3 h of hydrothermal treatment. All the diffraction peaks could be perfectly indexed to the tetragonal structure of BiOCl (JCPDS No. 6-249). However, the diffraction peak intensity of the (001) plane in these spectra was obviously stronger than that of the (110) plane, which was different from the sample prepared in 0.1 M mannitol. It indicated that the crystal had special anisotropic growth along the [001] direction. Fig. 5b and 5d showed the corresponding SEM images of the BiOCl products obtained in EG and DEG, which revealed that irregular sheet-like bulk BiOCl was fabricated in EG or DEG. Noticeably, when the reaction was carried out in deionized water, irregular sheet-like BiOCl was also obtained, as shown in Fig. 5f. Based on the experiment results, it illustrated that the mannitol played an important role in the formation of the square-like BiOCl nanoplates. It was believed that the physical and chemical properties of the solvent could influence the anisotropic growth of nanocrystals.^{30,35,38–40} We proposed that mannitol could function as a directing agent in the formation of square-like BiOCl nanoplates due to its long chain and

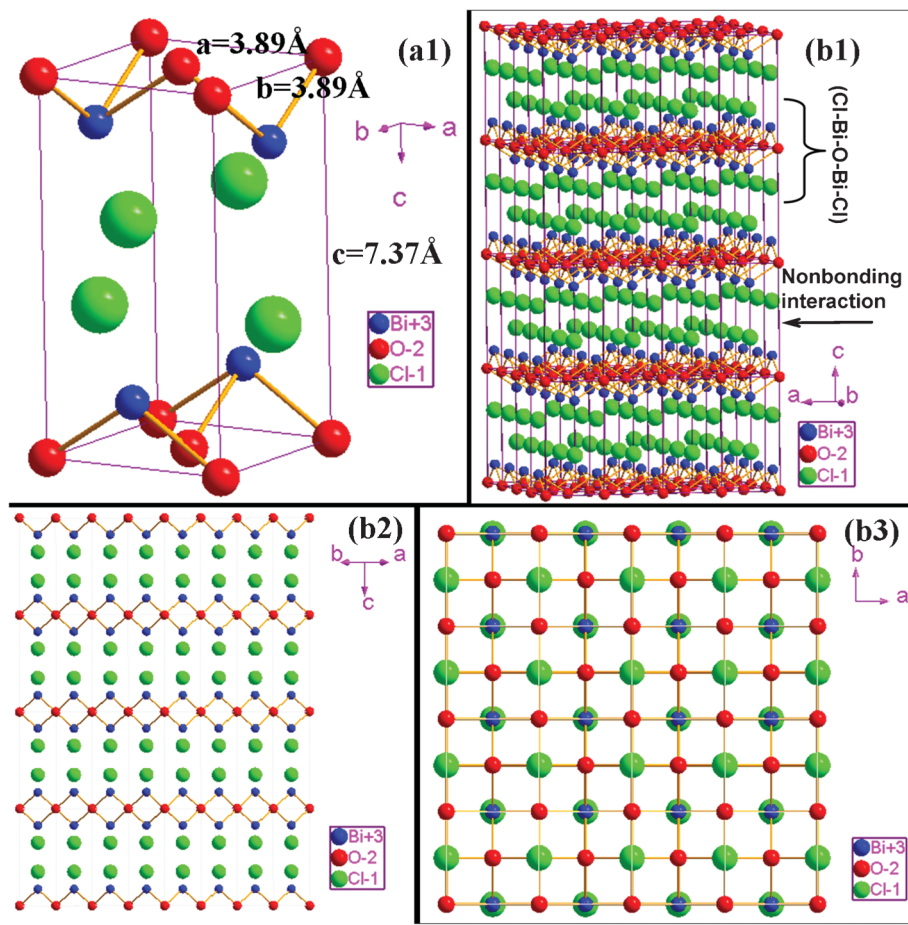


Fig. 3 Schematic structure model of BiOCl crystal ((a) unit cell, (b) $4 \times 4 \times 4$ cells) viewed from (1) three-dimensional projection, (2) [110] projection, (3) [001] projection.

polyhydroxyl of mannitol molecules. Mannitol molecules might selectively adsorb on the specific plane of BiOCl nuclei and restrict their intrinsic anisotropic growth, resulting in the formation of regular square-like nanoplates.

It was well known that the formation of specific nanostructures involved two steps: an initial nucleation stage and a crystal growth stage, which was a fast nucleation of amorphous primary particles followed by the slow aggregation and crystallization of primary particles.^{41–43} The growth process developed according to the crystal habit, which was associated with the energy of the exposed facets.^{41,44} Considering the spatial structure of BiOCl, it was reasonable to believe that the intrinsic anisotropic characteristics of BiOCl might dominate the shape of the primary BiOCl particles (such as the plate seed), and further affected the growth rate of the crystal along the crystalline planes because that the crystal facets tended to develop on the low index planes to minimize the surface energy during the growth of the crystal.^{15,45} Furthermore, the surfactants or capping agents could indirectly change the surface energies of the growing crystal facets, and the side facets may possess higher energy than top-bottom facets, thus leading to the formation of BiOCl nanoplates.

Based on the above results and analysis, the formation of square-like BiOCl nanoplates could be ascribed to the layered growth of BiOCl. It was proposed that the formation process of square-like BiOCl nanoplates might be divided into two steps:

nucleation and anisotropic growth (Scheme 2). Firstly, $\text{Bi}(\text{NO}_3)_3 \cdot 5\text{H}_2\text{O}$ was dissolved into 0.1 M mannitol solution and possibly formed a Bi-mannitol complex, which reacted with the large quantity of the Cl^- ion from the NaCl solution to form the BiOCl nuclei. Due to the special spatial structure of BiOCl, it was easy to fabricate the 2D laminar structure. BiOCl seeds vanished and had a tendency to form layered structures because of its $[\text{Cl}-\text{Bi}-\text{O}-\text{Bi}-\text{Cl}]$ layers during the hydrothermal process. Under the direction of mannitol molecules, the layered structure of BiOCl tended to a plate-growth for the fast growth along the [001] direction. The hydrogen bonding between hydroxyl groups and its selective adsorption also benefit to the formation to regular square-like nanoplates. Finally, well-crystallized square-like BiOCl nanoplates were formed by increasing reaction time to 3 h. It was also reported in the literature that anisotropic growth habit was employed to fabricate various 2D nanostructures,^{40,43,44,46} while surfactants and polymers could exert a remarkable level of the controlled growth of BiOCl nanoplate and were responsible for a range of BiOCl morphologies and structures.¹⁵

3.3 Optical properties and BET surface area

Generally, Raman spectroscopy is a powerful experimental technique for exploring the vibrational and structural properties of crystals. As a nondestructive approach for material characterization, it can be used to measure the symmetry of the

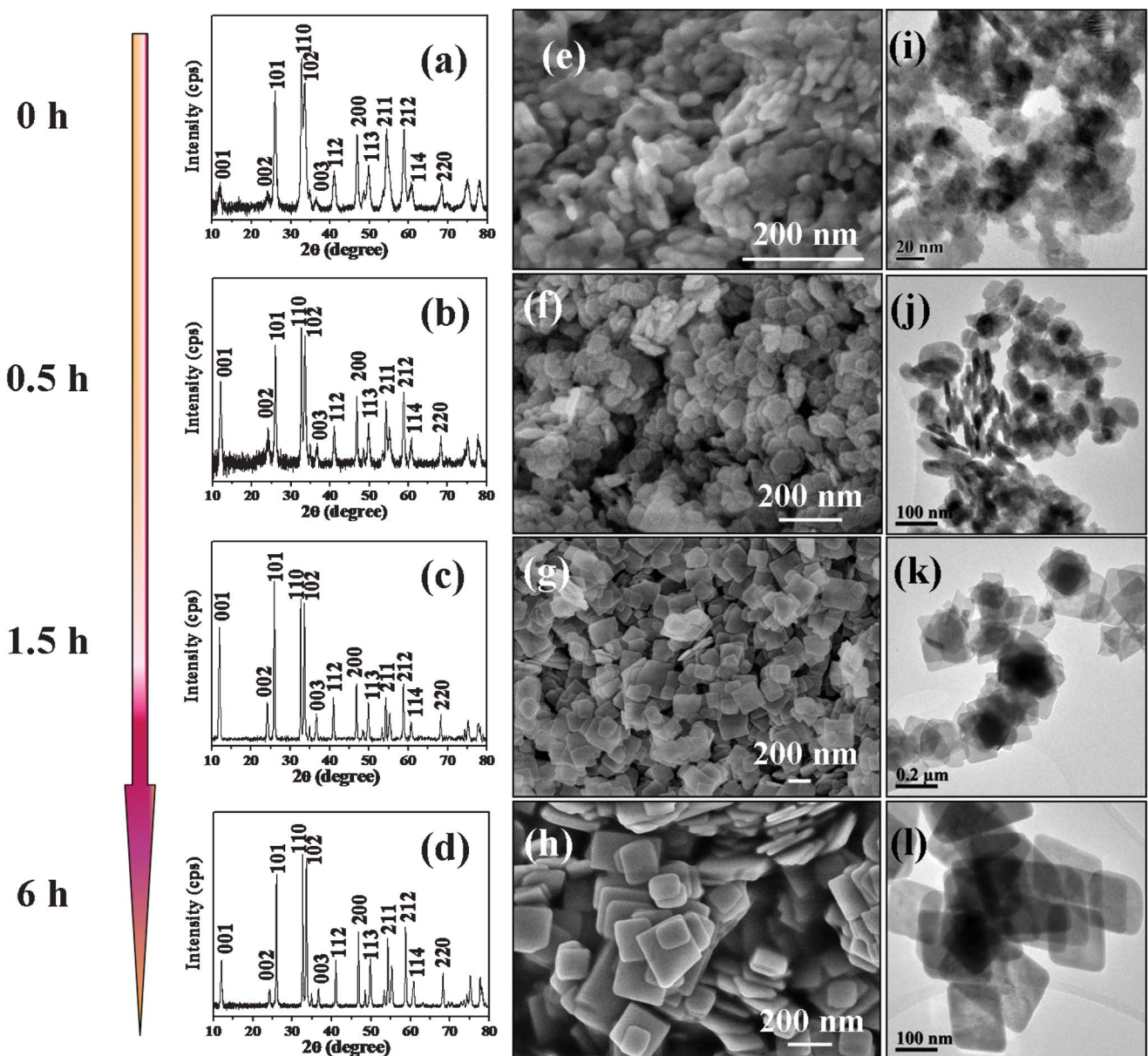


Fig. 4 XRD patterns (a–d), SEM images (e–h) and TEM images (i–l) of the BiOCl products obtained at different reaction times by the hydrothermal method in mannitol solution.

crystals and investigate the stress state in the materials. BiOCl has a tetragonal PbFCl⁻-type structure of space group P4/nmm (D_{4h}^7). For such a structure of space group D_{4h}^7 , with two molecular formulas per unit cell, the Raman active modes are two A_{1g} , B_{1g} , and E_g . The spectra of Fig. 6 consist of two distinguished bands and one weak band. Since symmetric vibrations usually give rise to more intense Raman bands than asymmetric vibrations, the strong band at 145 cm^{-1} was assigned to the A_{1g} internal Bi-Cl stretching mode. The A_{1g} produced by the external modes of Bi-Cl (60 cm^{-1})⁴⁷ was hard to detect due to the limit of the spectrophotometer. The band at 201 cm^{-1} could be assigned to the E_g internal Bi-Cl stretching mode, while the E_g external Bi-Cl stretching was probably masked by the strong Raman band at 145 cm^{-1} . The E_g and B_{1g} band, produced by the motion of the oxygen atoms at about 399 cm^{-1}

was very weak and not readily noticeable. The wavenumber here is similar to the reported values in literature²³ but is slightly smaller than that of powder BiOCl,⁴⁷ which probably attributed to the stronger orientation of the plate-like single crystal than that of the powders. In addition, as shown in the inset of Fig. 6, the peak intensity of the square-like nanoplates was remarkably weak compared with commercial BiOCl, which might be due to the decrease in the size of the nanoplates (Fig. S2, ESI†). The same phenomenon was also observed in the reported BiOCl nanostructures.^{15,18,26}

For semiconductor materials, diffuse reflectance spectroscopy (DRS) is a useful tool for characterizing the optical absorption property, which is recognized as one of the key factors for photocatalytic activities.^{3,48} The UV-vis diffuse reflectance spectra of as-synthesized square-like BiOCl nanoplates and

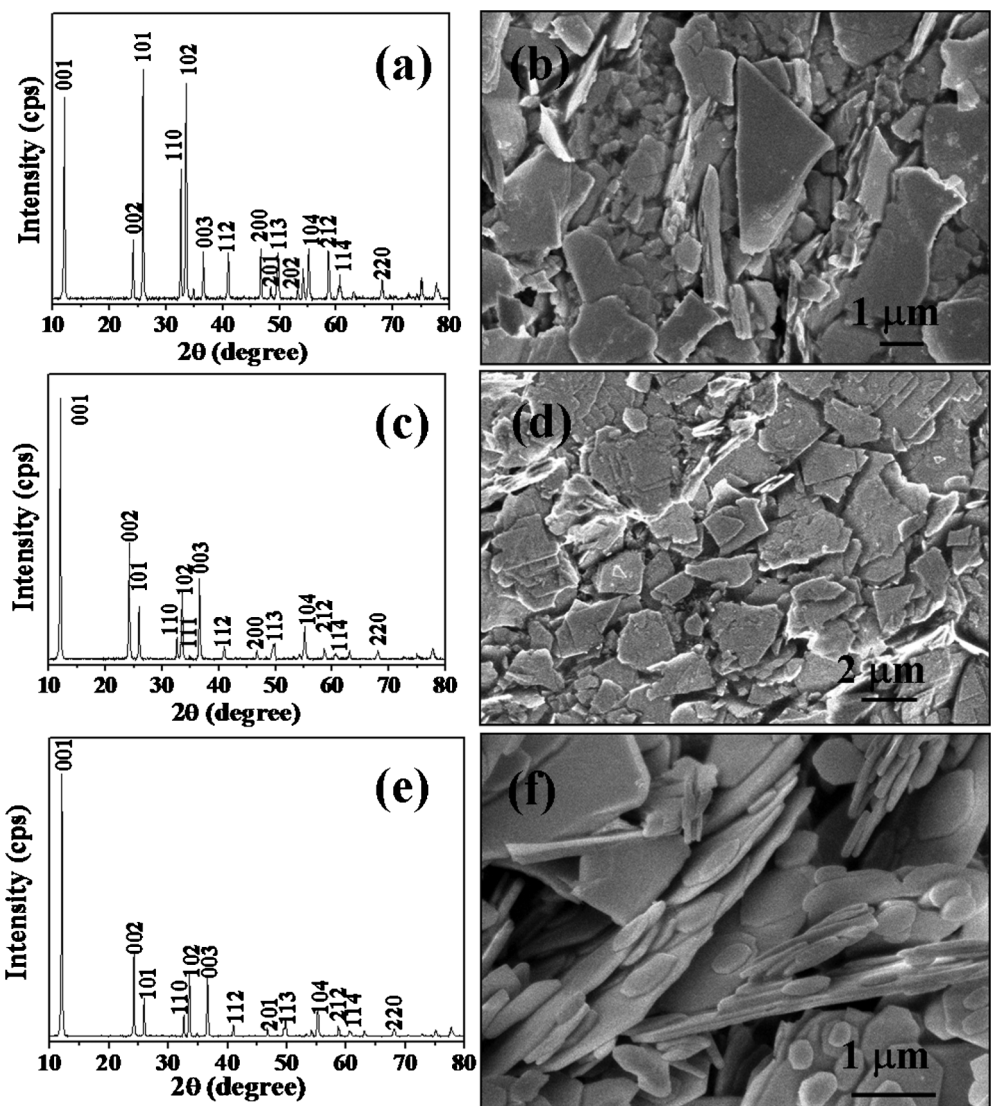
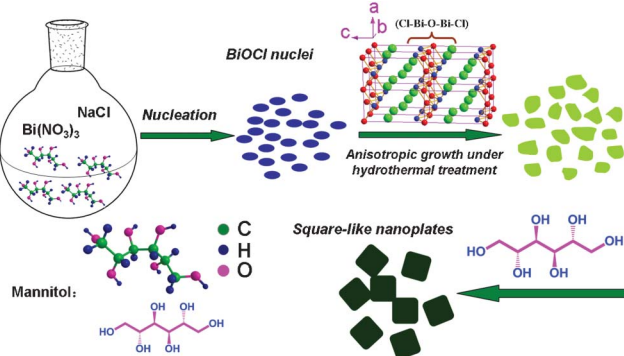


Fig. 5 XRD patterns (a, c and e) and SEM images (b, d and f) of BiOCl products synthesized by hydrothermal method in different solvents: EG (a and b), DEG (c and d) and H₂O (e and f).

commercial BiOCl were shown in Fig. 7a, the steep shape of the spectra decrease around 380 nm indicated that the absorption was due to the band gap transition. As a crystalline semiconductor, the optical absorption near the band edge follows the

formula $\alpha h\nu = A (h\nu - E_g)^{n/2}$, where α , v , E_g , and A are the absorption coefficient, light frequency, band gap energy, and a constant, respectively. Among them, n depends on the



Scheme 2 Illustration of the possible formation mechanism of square-like BiOCl nanoplates.

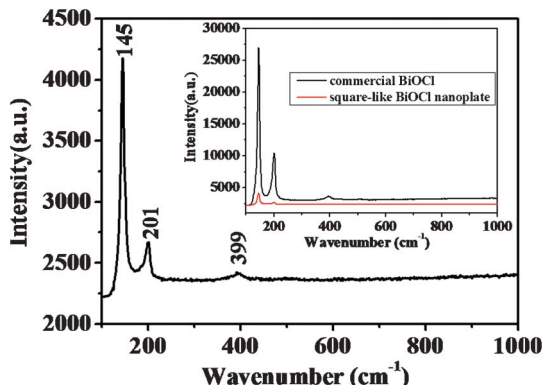


Fig. 6 Raman spectra of the as-synthesized square-like BiOCl nanoplates and commercial BiOCl.

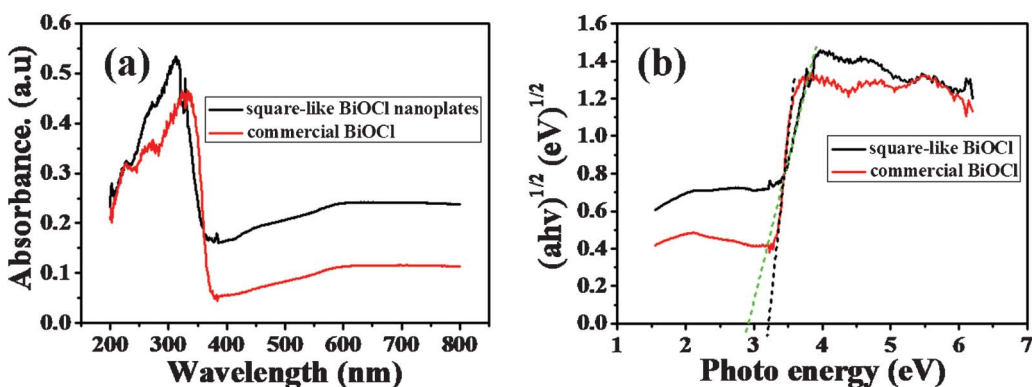


Fig. 7 UV-vis diffuse reflectance spectra (DRS) of the as-synthesized square-like BiOCl nanoplates and commercial BiOCl (a) and plots of $(\alpha h v)^{1/2}$ versus the photon energy ($h v$) for the as-synthesized square-like BiOCl nanoplates and commercial BiOCl (b).

characteristics of the transition in a semiconductor (*i.e.*, $n = 1$ for direct transition or $n = 4$ for indirect transition). According to the equation, the value of n was estimated to be 4, indicating of indirect transition of the BiOCl powders.⁷ The band gap energies (E_g values) of the BiOCl samples could be thus estimated from a plot of $(\alpha h v)^{1/2}$ versus the photon energy ($h v$). The intercept of the tangent to the x -axis will give a good approximation of the band gap energies for the BiOCl powders. Plots of $(\alpha h v)^{1/2}$ versus photon energy ($h v$) of BiOCl powders were shown in Fig. 7b. The estimated band gap energies of the resulting samples were about 2.92 and 3.21 eV for square-like and commercial BiOCl, respectively. The square-like BiOCl nanoplates have a narrower band gap, which was different from the theoretic value (3.46 eV).⁴⁹ It is well known that the structure, morphology and size of the semiconductor nanostructures have an important influence on related optical properties and offer a way of tuning the band gap as a result.^{21,50,51} In addition, Hilmi Ünlü also reported that the decrease in the bandgap energies of diamond semiconductors with increasing temperature was shown to be caused by the interaction of the free electrons, holes and recombined electron-hole pairs with lattice phonons and linear expansion of the lattice constant.⁵² According to Ünlü's study, the decrease in the band gap of square-like BiOCl nanoplates could also be explained with phonon confinement effects. When the sizes and dimensionality of samples were reduced, phonon confinement effects would occur.^{53–55} Namely, some Raman scattering of nanostructured materials was shifted to higher or

lower frequencies, so the phonons were confined.^{56–58} Therefore, the phonon confinements could influence the decrease or increase in the bandgap energies of the nanostructured materials. In this study, the phonon confinement effects resulted in a decrease of the band gap of square-like BiOCl nanoplates compared with commercial BiOCl. However, our understanding is still limited and further work will include investigation on the shape- and size-dependent optical absorption properties of BiOCl nanostructures.

To be a good candidate for a photocatalyst, its specific surface area is also important. Normally, the larger surface area of the catalyst will result in higher photocatalytic activity.⁵⁹ The Brunauer–Emmett–Teller (BET) specific surface area of synthesized BiOCl square-like nanoplates was investigated by nitrogen adsorption-desorption measurements. Fig. 8 showed the nitrogen adsorption-desorption isotherms of square-like and commercial BiOCl. The BET surface areas of the square-like and commercial BiOCl calculated from the results of N₂ adsorption were 8.1 and 0.2 m² g⁻¹, respectively. The value of the square-like BiOCl nanoplates was more than 40 times larger than that of commercial BiOCl powder.

3.4 Photocatalytic activity under visible light and possible mechanism

The photocatalytic activities of the as-synthesized square-like BiOCl nanoplates were evaluated by the degradation of RhB

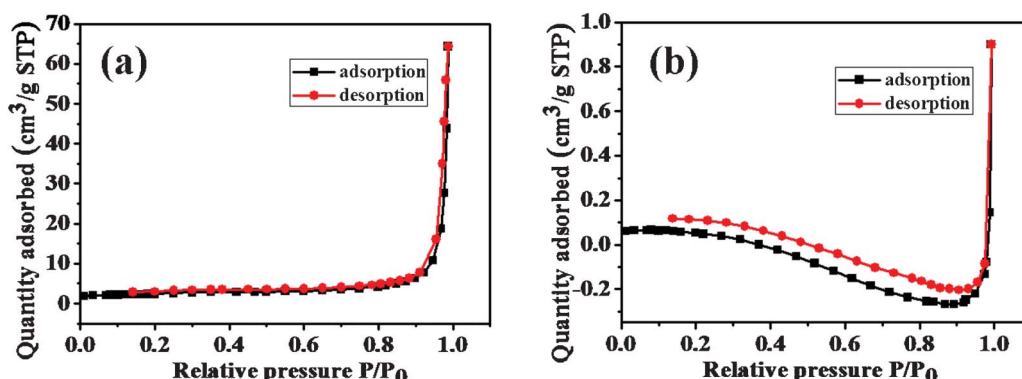


Fig. 8 Nitrogen adsorption-desorption isotherms of the as-synthesized square-like BiOCl nanoplates (a) and commercial BiOCl (b).

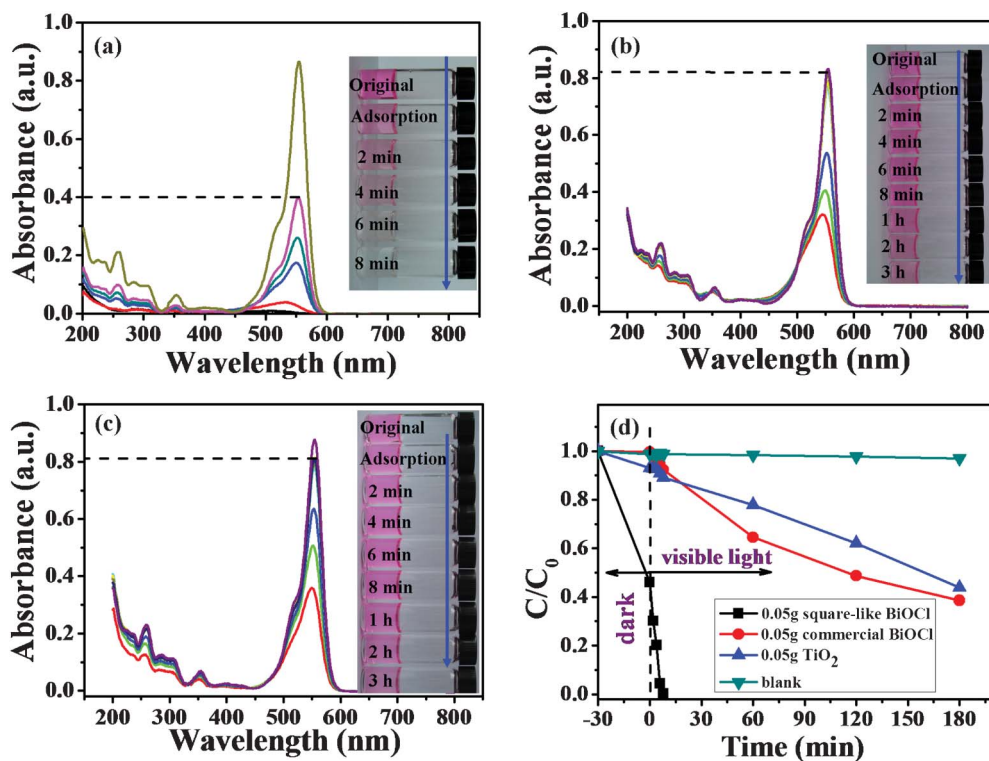


Fig. 9 The temporal evolution of the spectra and the photograph images of the RhB solution in the presence of 0.05 g of different photocatalysts under visible light irradiation: square-like BiOCl nanoplates (a), commercial BiOCl (b) and anatase TiO₂ (c); The variation of RhB concentrations (C/C_0) with irradiation time over different photocatalysts and photolysis of RhB (d).

solution under visible light irradiation of a 500 W Xe lamp with a 400 nm cutoff filter ($\lambda > 400$ nm) after the adsorption-desorption equilibrium between the BiOCl sample and RhB. The UV-vis spectra and photograph images of RhB at different irradiation time over square-like BiOCl nanoplates (0.05 g) are illustrated in Fig. 9a. It showed that the absorption peak at 554 nm decreased dramatically as the exposure time increased, and completely disappeared within 8 min. For comparison, direct photolysis of RhB and RhB degradation with a small amount of different photocatalysts including the commercial BiOCl, and TiO₂ (anatase) were performed under identical conditions. Fig. 9b–9c displayed the temporal evolution of the spectra and photograph images during the photodegradation of RhB in the presence of 0.05 g different catalysts under visible light irradiation, and Fig. 9d showed the variation in RhB concentrations (C/C_0) with irradiation time over different photocatalysts, where C_0 is the initial concentration of RhB and C is the concentration of RhB at t time. It was clearly observed that the RhB concentration hardly changed with the increase of irradiation time in the absence of catalysts, while the photocatalytic degradation efficiency was only 61% and 56% for commercial BiOCl and TiO₂, respectively, after 3 h visible light irradiation. It indicated that the square-like BiOCl nanoplates exhibited the highest photocatalytic activity compared with that of the commercial BiOCl and TiO₂ (anatase) under visible light irradiation.

It was also found that nearly 55% RhB was adsorbed by the square-like BiOCl nanoplates in the dark equilibration, and less than 10% dye adsorption was observed for commercial BiOCl and TiO₂, indicating the strong dye adsorption ability of

square-like BiOCl nanoplates. To systematically investigate the dye adsorption performance of the square-like BiOCl nanoplates, different amounts of square-like BiOCl nanoplates were used for the photocatalytic degradation of RhB under the same conditions. Fig. 10 showed the temporal evolution of the UV-vis spectra changes and concentrations variation (C/C_0) of RhB with irradiation time over different amounts of square-like BiOCl nanoplates (0.01, 0.03, 0.05 and 0.1 g). In the absence of light, only an adsorption process took place. As shown in Fig. 10, the amount of dye adsorption was obviously different in the presence of different amounts of BiOCl photocatalyst. After dark equilibration, RhB adsorption of 0.01 g BiOCl nanoplates was only 11%, which could be negligible. But the adsorption became apparent by increasing the amount of BiOCl nanoplates, the highest dye adsorption was 77.8% for 0.1 g of the BiOCl photocatalyst. The color of the BiOCl powder changed from white to pink at the end of the dark experiment. It illustrated that the square-like BiOCl nanoplates have excellent adsorption capability for organic dye. When the light source was switched on, the photocatalytic reaction ensued. The RhB dye in the 0.1 g BiOCl nanoplates suspension was degraded completely within 4 min of irradiation. In the 0.03 g BiOCl nanoplate dispersion, the RhB solution was completely decolorized within 20 min. Only 90% of RhB removal was observed in the presence of 0.01 g BiOCl nanoplates after 120 min irradiation.

It was noticeable that RhB dye was only adsorbed on the surface of BiOCl nanoplates in the dark equilibration, and was not degraded by BiOCl photocatalyst and was confirmed by the color changes of 0.1 g of BiOCl powders after dark equilibration

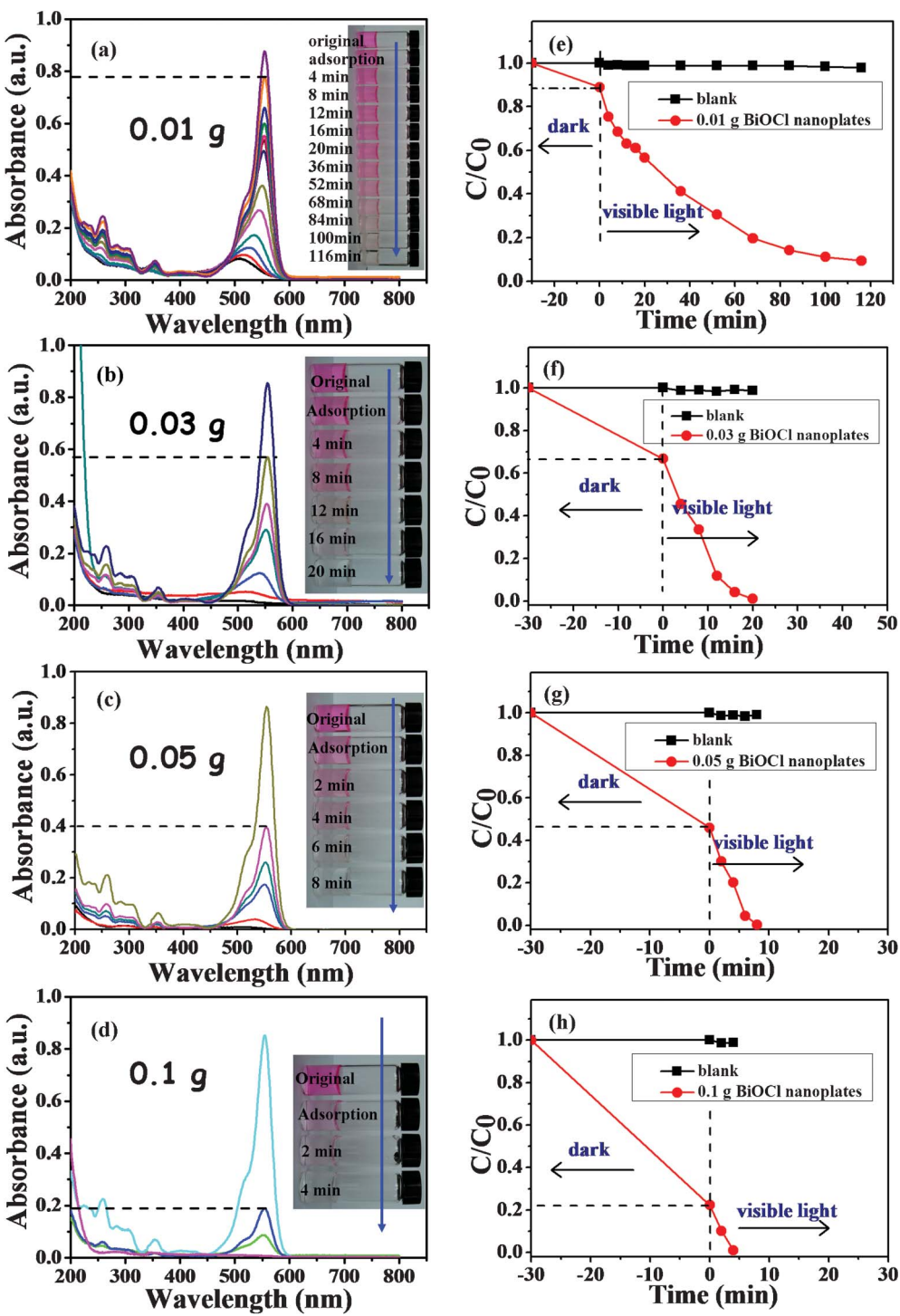


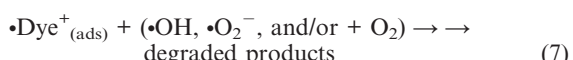
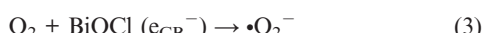
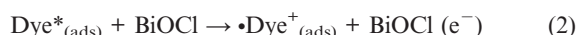
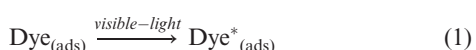
Fig. 10 The temporal evolution of UV-vis spectra and photographic images of the RhB solution (a–d) and the variation of RhB concentrations (C/C_0) with irradiation time (e–h) over different amounts of square-like BiOCl nanoplates under visible light irradiation.

and complete photodegradation, (Fig. S3, ESI†). Although the color of the RhB solution faded, the BiOCl nanoplates became pink after dye adsorption in the dark. However, both the RhB solution and BiOCl nanoplates decolorized after 4 min visible light irradiation. In the absence of visible light, the RhB solution remained pink even after 96 h in dark equilibrium. Considering that the photocatalysis reactions mainly took place at the surface of the catalysts rather than in the bulk, the adsorption capability

of the BiOCl was a key factor for the decomposition of the dyes. The square-like BiOCl nanoplates also showed good stability in the photocatalytic reaction, which was confirmed by the XRD pattern of the sample after photodegradation. No change in the BiOCl crystal structure was observed (Fig. S4, ESI†).

In fact, BiOCl nanoplates can only absorb UV light ($\lambda < 390$ nm) due to its UV-vis diffuse reflectance edges (Fig. 7). Hence, visible light ($\lambda > 400$ nm) could not excite BiOCl to produce reactive

radicals because of its wide band gap, and RhB degradation by BiOCl through a photocatalytic pathway was negligible. On the other hand, direct photolysis of RhB under visible light also didn't occur, as demonstrated by the blank experiment. It was proposed that RhB degradation on square-like BiOCl nanoplates mainly proceeded along a photosensitization pathway under visible light irradiation. In the photosensitization pathway, RhB dye was considered a photosensitizer,⁶⁰ whereas the BiOCl nanoplates played the key roles of electron carriers and electron acceptors. As illustrated in Scheme 3, BiOCl nanoplates do not directly absorb light under visible light illumination. The adsorbed RhB dye molecules absorbed the light energy to produce singlet and triplet states (denoted here simply as RhB^{*}_(ads)) and the electron injection from the excited states of the adsorbed dye molecules (RhB^{*}_(ads)) into the conduction band of BiOCl resulted in the conversion of RhB to the radical cation •RhB⁺ and formation of BiOCl (e⁻). Then, BiOCl (e⁻) reacted with the surface-adsorbed O₂ molecules to yield reactive oxygen radicals containing •O₂⁻ and •OH. The radical cation •RhB⁺ ultimately reacted with reactive oxygen radicals and/or molecular oxygen to yield the degraded products.^{5,60,61} The process is described in detail below:



It is known that a dye photosensitization mechanism is closely related to the dye structural stability, the dye absorbance and the adsorption capability of photocatalyst.^{10,62} Because catalyst-assisted photocatalytic dye degradation under visible irradiation requires direct interaction between the dyes and the surface of the catalyst to achieve an efficient charge injection, the increase

in both the dye adsorption amount and strength could promote the electron transfer from the excited dyes to catalyst.^{60,61,63,64} Such a rapid electron injection offered more opportunities for the conduction band transport of injected electrons to surface reaction sites and the reaction of oxidized dyes. Therefore, the strong dye adsorption performance of square-like BiOCl nanoplates could promote both the adsorption amount and adsorption strength for RhB dye, which allowed more efficient transport for the injected electrons from the excited RhB^{*}_(ads) to BiOCl nanoplates, leading to an enhancement of the photocatalytic performance. The dye photosensitization mechanism provided another promising strategy for the semiconductors with a wide band gap to harvest visible light and extend its photo-response to visible region, which was also associated with the good photosensitized degradation performance of NaY(MoO₄)₂⁶⁵ and graphene-gold nanocomposites⁶⁶ reported in the literatures.

Another reason of remarkable photocatalytic activity of BiOCl, is mainly ascribed to its layered structure. As shown in Fig. 3, the [BiOCl] layers are stacked together by the Van der Waals forces (nonbonding interaction) through the Cl atoms along the *c*-axis. Thus, the structure is not closely packed in this direction. When one electron is excited by one photon from the Cl 3p state to 6p state in BiOCl, one pair of a hole and an excited electron appear.⁷ The layered BiOCl structure can provide sufficient space to polarize the related atoms and orbitals. The induced dipole can enable the effective separation of the photoinduced electron-hole pairs, assisting a high photocatalytic activity. Therefore, the excellent visible-light-driven photocatalytic activity of square-like BiOCl nanoplates could be mainly attributed to its layered structure, strong RhB dye adsorption upon the surface and the dye photosensitization mechanism.

4. Conclusion

In summary, well-crystallized BiOCl nanoplates with square-like morphology were successfully synthesized *via* an effective and environmentally friendly hydrothermal route in mannitol solution. By varying the reaction time and solvent, the possible formation mechanism which involved the process of layered growth was proposed. It was found that mannitol played a key role in the formation of BiOCl nanoplates. The square-like BiOCl nanoplates exhibited excellent visible-light-driven photocatalytic efficiency, which was much higher than that of commercial BiOCl and TiO₂ (anatase). The high visible-light photocatalytic activity was mainly attributed to a synergistic effect of the layered structure and the strong adsorption of RhB dye upon the BiOCl nanoplates, which might allow more efficient transport of the injected electrons. A possible dye-sensitized photocatalytic degradation process (photosensitization pathway) was proposed. The present work not only provides a new route to fabricate 2D BiOCl nanostructures, but also develops new promising visible-light-driven photocatalysts and implements efficient applications, both in sunlight and artificial light for the degradation of dye pollutants.

Acknowledgements

This work was supported by the National Natural Science Foundation of China (Grants 20801043 and 21171136), the

Scheme 3 Proposed photodegradation mechanism of RhB under visible light irradiation.

Program for New Century Excellent Talents in University (NCET-09-0136), Wuhan Chenguang Scheme (Grant 200850731376) established under Wuhan Science and Technology Bureau. We thank Mr. Frankie Y. F. Chan for the kindly help in TEM characterizations and Dr J. Q. Ning for the kindly help in Raman spectra measurement.

References

- A. Mills, R. H. Davies and D. Worsley, *Chem. Soc. Rev.*, 1993, **22**, 417.
- M. R. Hoffmann, S. T. Martin, W. Choi and D. W. Bahnemann, *Chem. Rev.*, 1995, **95**, 69.
- J. Tang, Z. Zou and J. Ye, *Angew. Chem., Int. Ed.*, 2004, **43**, 4463.
- N. Wu, J. Wang, D. N. Tafen, H. Wang, J.-G. Zheng, J. P. Lewis, X. Liu, S. S. Leonard and A. Manivannan, *J. Am. Chem. Soc.*, 2010, **132**, 6679.
- C. Chen, W. Ma and J. Zhao, *Chem. Soc. Rev.*, 2010, **39**, 4206.
- J. Hou, Y. Qu, D. Krsmanovic, C. Ducati, D. Eder and R. V. Kumar, *J. Mater. Chem.*, 2010, **20**, 2418.
- K.-L. Zhang, C.-M. Liu, F.-Q. Huang, C. Zheng and W.-D. Wang, *Appl. Catal., B*, 2006, **68**, 125.
- X. Zhang, Z. Ai, F. Jia and L. Zhang, *J. Phys. Chem. C*, 2008, **112**, 747.
- X. Chang, J. Huang, C. Cheng, Q. Sui, W. Sha, G. Ji, S. Deng and G. Yu, *Catal. Commun.*, 2010, **11**, 460.
- X. Lin, T. Huang, F. Huang, W. Wang and J. Shi, *J. Phys. Chem. B*, 2006, **110**, 24629.
- X. Lin, T. Huang, F. Huang, W. Wang and J. Shi, *J. Mater. Chem.*, 2007, **17**, 2145.
- H. Deng, J. Wang, Q. Peng, X. Wang and Y. Li, *Chem.-Eur. J.*, 2005, **11**, 6519.
- S. Wu, C. Wang, Y. Cui, T. Wang, B. Huang, X. Zhang, X. Qin and P. Brault, *Mater. Lett.*, 2010, **64**, 115.
- C. Wang, C. Shao, Y. Liu and L. Zhang, *Scr. Mater.*, 2008, **59**, 332.
- Y. Lei, G. Wang, S. Song, W. Fan and H. Zhang, *CrystEngComm*, 2009, **11**, 1857.
- J. Ma, X. Liu, J. Lian, X. Duan and W. Zheng, *Cryst. Growth Des.*, 2010, **10**, 2522.
- Z. Deng, D. Chen, B. Peng and F. Tang, *Cryst. Growth Des.*, 2008, **8**, 2995.
- J. Geng, W.-H. Hou, Y.-N. Lv, J.-J. Zhu and H.-Y. Chen, *Inorg. Chem.*, 2005, **44**, 8503.
- L. Ye, L. Zan, L. Tian, T. Peng and J. Zhang, *Chem. Commun.*, 2011, **47**, 6951.
- Y. Li, J. Liu, J. Jiang and J. Yu, *Dalton Trans.*, 2011, **40**, 6632.
- L.-P. Zhu, G.-H. Liao, N.-C. Bing, L.-L. Wang, Y. Yang and H.-Y. Xie, *CrystEngComm*, 2010, **12**, 3791.
- J.-M. Song, C.-J. Mao, H.-L. Niu, Y.-H. Shen and S.-Y. Zhang, *CrystEngComm*, 2010, **12**, 3875.
- S. Cao, C. Guo, Y. Lv, Y. Guo and Q. Liu, *Nanotechnology*, 2009, **20**, 275702.
- F. A. Banniste, *Mineral. Mag.*, 1935, **24**, 49.
- N. Kijima, K. Matano, M. Saito, T. Oikawa, T. Konishi, H. Yasuda, T. Sato and Y. Yoshimura, *Appl. Catal., A*, 2001, **206**, 237.
- L. Zhu, Y. Xie, X. Zheng, X. Yin and X. Tian, *Inorg. Chem.*, 2002, **41**, 4560.
- C. F. Guo, S. Cao, J. Zhang, H. Tang, S. Guo, Y. Tian and Q. Liu, *J. Am. Chem. Soc.*, 2011, **133**, 8211.
- H. Katsuki and S. Komarneni, *J. Am. Ceram. Soc.*, 2001, **84**, 2313.
- S. Komarneni, D. Li, B. Newalkar, H. Katsuki and A. S. Bhalla, *Langmuir*, 2002, **18**, 5959.
- Z. Liu, J. Liang, S. Li, S. Peng and Y. Qian, *Chem.-Eur. J.*, 2004, **10**, 634.
- H.-P. Cong and S.-H. Yu, *Cryst. Growth Des.*, 2009, **9**, 210.
- Q. Lu, F. Gao and S. Komarneni, *J. Am. Chem. Soc.*, 2004, **126**, 54.
- Q. Lu, F. Gao and S. Komarneni, *Chem. Mater.*, 2006, **18**, 159.
- M. Shang, W. Wang and H. Xu, *Cryst. Growth Des.*, 2009, **9**, 991.
- G. Cheng, H. Yang, K. Rong, Z. Lu, X. Yu and R. Chen, *J. Solid State Chem.*, 2010, **183**, 1878.
- J. Xiong, G. Cheng, Z. Lu, J. Tang, X. Yu and R. Chen, *CrystEngComm*, 2011, **13**, 2381.
- J. Wu, F. Qin, G. Cheng, H. Li, J. Zhang, Y. Xie, H.-J. Yang, Z. Lu, X. Yu and R. Chen, *J. Alloys Compd.*, 2011, **509**, 2116.
- W. S. Sheldrick and M. Wachhold, *Angew. Chem., Int. Ed. Engl.*, 1997, **36**, 206.
- Y. Xu, N. Al-Salim, C. W. Bumby and R. D. Tilley, *J. Am. Chem. Soc.*, 2009, **131**, 15990.
- Y. C. Cao, *J. Am. Chem. Soc.*, 2004, **126**, 7456.
- Z. A. Peng and X. Peng, *J. Am. Chem. Soc.*, 2002, **124**, 3343.
- B. L. Cushing, V. L. Kolesnichenko and C. J. O'Connor, *Chem. Rev.*, 2004, **104**, 3893.
- W. Du, X. Qian, X. Ma, Q. Gong, H. Cao and J. Yin, *Chem.-Eur. J.*, 2007, **13**, 3241.
- C. Zhang and Y. Zhu, *Chem. Mater.*, 2005, **17**, 3537.
- R. Jin, Y. Charles Cao, E. Hao, G. S. Metraux, G. C. Schatz and C. A. Mirkin, *Nature*, 2003, **425**, 487.
- G. Xi and J. Ye, *Chem. Commun.*, 2010, **46**, 1893.
- J. E. D. Davies, *J. Inorg. Nucl. Chem.*, 1973, **35**, 1531.
- Y. Lei, G. Wang, S. Song, W. Fan, M. Pang, J. Tang and H. Zhang, *Dalton Trans.*, 2010, **39**, 3273.
- H. Peng, C. K. Chan, S. Meister, X. F. Zhang and Y. Cui, *Chem. Mater.*, 2009, **21**, 247.
- L. Li, J. Hu, W. Yang and A. P. Alivisatos, *Nano Lett.*, 2001, **1**, 349.
- G. Dukovic, F. Wang, D. Song, M. Y. Sfeir, T. F. Heinz and L. E. Brus, *Nano Lett.*, 2005, **5**, 2314.
- H. Ünlü, *Solid-State Electron.*, 1992, **35**, 1343.
- S. Sahoo, S. Dhara, S. Mahadevan and A. Arora, *J. Nanosci. Nanotechnol.*, 2009, **9**, 5604.
- S. Sahoo, S. Dhara, V. Sivasubramanian, S. Kalavathi and A. Arora, *J. Raman Spectrosc.*, 2009, **40**, 1050.
- A. K. Arora, M. Rajalakshmi, T. R. Ravindran and V. Sivasubramanian, *J. Raman Spectrosc.*, 2007, **38**, 604.
- R. S. Devan, W.-D. Ho, S. Y. Wu and Y.-R. Ma, *J. Appl. Crystallogr.*, 2010, **43**, 498.
- L. Kumari, Y.-R. Ma, C.-C. Tsai, Y.-W. Lin, S. Y. Wu, K.-W. Cheng and Y. Liou, *Nanotechnology*, 2007, **18**, 115717.
- Y. R. Ma, C. M. Lin, C. L. Yeh and R. T. Huang, *J. Vac. Sci. Technol., B*, 2005, **23**, 2141.
- M. A. Fox and M. T. Dulay, *Chem. Rev.*, 1993, **93**, 341.
- T. Wu, G. Liu, J. Zhao, H. Hidaka and N. Serpone, *J. Phys. Chem. B*, 1998, **102**, 5845.
- J. Zhao, T. Wu, K. Wu, K. Oikawa, H. Hidaka and N. Serpone, *Environ. Sci. Technol.*, 1998, **32**, 2394.
- W. S. Kuo and P. H. Ho, *Dyes Pigm.*, 2006, **71**, 212.
- A. Heller, *Acc. Chem. Res.*, 1995, **28**, 503.
- A. Hagfeldt and M. Graetzel, *Chem. Rev.*, 1995, **95**, 49.
- S.-S. Liu, D.-P. Yang, D.-K. Ma, S. Wang, T.-D. Tang and S.-M. Huang, *Chem. Commun.*, 2011, **47**, 8013.
- Z. Xiong, L. L. Zhang, J. Ma and X. S. Zhao, *Chem. Commun.*, 2010, **46**, 6099.